https://doi.org/10.5194/angeo-2023-14
Preprint. Discussion started: 11 May 2023

Annales Geophysicae
Discussions
Open Access

The Local Bow Shock Environment during Magnetosheath Jet Formation: Results from a Hybrid-Vlasov Simulation

Jonas Suni[1], Minna Palmroth[1,2], Lucile Turc[1], Markus Battarbee[1], Giulia Cozzani[1], Maxime Dubart[1], Urs Ganse[1], Harriet George[3], Evgeny Gordeev[1], Konstantinos Papadakis[1], Yann Pfau-Kempf[1], Vertti Tarvus[1], Fasil Tesema[1], and Hongyang Zhou[1]

[1]Department of Physics, University of Helsinki, Helsinki, Finland
[2]Space and Earth Observation Centre, Finnish Meteorological Institute, Helsinki, Finland
[3]Laboratory for Atmospheric and Space Physics, University of Colorado Boulder, Colorado, USA

Correspondence: Jonas Suni (jonas.suni@helsinki.fi)

Abstract.

Magnetosheath jets are plasma structures that are characterised by enhanced dynamics pressure and/or plasma velocity. A jet generation mechanism that has been widely discussed in observational and numerical studies is steepened Ultra Low Frequency (ULF) waves interacting with the bow shock. However, other formation mechanisms have also been proposed. In Suni et al. (2021), we studied jets in four 2D simulation runs of the global magnetospheric hybrid-Vlasov model Vlasiator and found that 75% of the jets were associated with regions of enhanced magnetic field and dynamic pressure in the foreshock that we called foreshock compressive structures (FCS). In this study we focus on investigating the jets in the same simulation runs that are not associated with FCSs (non-FCS-jets), and then compare them to FCS-associated jets (FCS-jets). The data set consists of 791 jets in total, of which 562 (71%) are FCS-jets and 229 (29%) are non-FCS-jets. We find that the non-FCS-jets can be divided into two categories based on their direction of propagation, either predominantly antisunward or predominantly towards the flanks of the magnetosphere. Using this new categorisation methodology, we compare the plasma and magnetic field properties of flankward-propagating jets, antisunward-propagating jets, and FCS-jets at and around their formation times and locations, using both case studies and statistical analysis. We find that 120 (52%) of the non-FCS-jets propagate antisunward, are associated with dynamic pressure and magnetic field enhancements in the foreshock, and are very reminiscent of FCS-jets in their properties. Thus 86% of the jets in the data set are associated with dynamic pressure and magnetic field enhancements in the foreshock. The remaining 109 (48%) propagate toward the flanks and exhibit higher perpendicular than parallel temperature with respect to the magnetic field, suggesting that they could consist of quasi-perpendicular magnetosheath plasma. We propose that these jets could be associated with local turning of the shock geometry from quasi-parallel to quasi-perpendicular due to bow shock reformation at the oblique shock caused by foreshock ULF wave activity. As antisunward-propagating jets can potentially impact the magnetopause and have effects on the magnetosphere, understanding which foreshock and bow shock phenomena are associated with them and which are not is important.

https://doi.org/10.5194/angeo-2023-14
Preprint. Discussion started: 11 May 2023

1 Introduction

When the supermagnetosonic solar wind interacts with Earth's magnetic field, a bow shock forms ahead of the Earth. The part of the shock where the interplanetary magnetic field (IMF) is roughly parallel to the shock normal direction is called the quasi-parallel bow shock. The part where the IMF is roughly perpendicular to the shock normal direction is known as the quasi-perpendicular bow shock. Earthward of the IMF field line tangential to the bow shock, solar wind particles can be reflected by the bow shock and travel back upstream along magnetic field lines and interact with the pristine solar wind, causing a foreshock to form (e.g. Eastwood et al., 2005b; Wilson, 2016). The part of the foreshock containing reflected electrons is called the electron foreshock, and its sunward edge is close to the tangential field line. The edge of the ion foreshock, which contains field-aligned electron and ion beams but exhibits no wave activity, is earthward of the electron foreshock edge. The interaction between the solar wind and the reflected ions generates Ultra Low Frequency (ULF) waves via the ion-ion beam right-hand instability (Gary, 1991). The waves are advected back toward the bow shock by the solar wind flow. The part of the foreshock containing these ULF waves along with suprathermal electrons and ions is known as the ULF foreshock (Eastwood et al., 2005b; Andrés et al., 2015), and because the wave generation requires a finite time dictated by the instability growth rate (Blanco-Cano et al., 2009), the edge of the ULF foreshock – the ULF foreshock boundary – is earthward of the ion foreshock edge.

As the solar wind plasma traverses the bow shock, it is compressed, heated, and decelerated. The region of space where this shocked plasma flows around Earth's magnetosphere is known as Earth's magnetosheath (e.g. Lucek et al., 2005). The boundary between the magnetosheath and the magnetosphere is called the magnetopause. As with the bow shock, the magnetosheath can also be divided into two subregions. The part of the magnetosheath downstream of the quasi-parallel bow shock is known as the quasi-parallel magnetosheath. The ULF waves generated in the foreshock can be transmitted through the bow shock into the quasi-parallel magnetosheath, causing it to also be dynamic (e.g. Dimmock et al., 2014; Turc et al., 2023). The part of the magnetosheath downstream of the quasi-perpendicular shock is called the quasi-perpendicular magnetosheath.

The dynamic quasi-parallel magnetosheath is host to many kinds of transient phenomena (Zhang et al., 2022). One such phenomenon is magnetosheath jets. They were first observed by spacecraft in 1996 (Němeček et al., 1998) and have since then been described in many observational studies (e.g. Savin et al., 2008; Amata et al., 2011; Dmitriev and Suvorova, 2015; Hietala and Plaschke, 2013; Plaschke et al., 2017, 2020; Gunell et al., 2014; Gutynska et al., 2015; Plaschke and Hietala, 2018; Wang et al., 2018; Goncharov et al., 2020; Raptis et al., 2022b) as well as in simulations (e.g. Karimabadi et al., 2014; Hao et al., 2016; Omidi et al., 2016; Palmroth et al., 2018b; Omelchenko et al., 2021). Magnetosheath jets are usually defined as structures or regions of enhanced dynamic pressure $P_{\mathrm{dyn}} = \rho_m v^2$, where ρ_m is the mass density and v the bulk speed of the plasma, in the magnetosheath, though specific definitions and terminology differ from study to study (see Plaschke et al., 2018). The "transient flux enhancements" studied by Němeček et al. (1998) were defined as enhancements of ion flux in the magnetosheath, while Hietala et al. (2012) defined "supermagnetosonic jets" as regions where the magnetosheath flow is supermagnetosonic. Karlsson et al. (2012, 2015) studied "plasmoids," regions of enhanced magnetosheath density, while Plaschke et al. (2013) defined "high speed jets" using the enhancement of x-directional dynamic pressure. In this study we employ the definition of Archer and Horbury (2013), whose "dynamic pressure enhancements" are defined as regions where the dynamic pressure in the magnetosheath is at least twice the time-average of the magnetosheath dynamic pressure. This definition was deemed to be most appropriate in previous studies using the same simulation data as this study (Palmroth et al., 2021; Suni et al., 2021), as it is based on dynamic pressure and only captures transient structures.

Magnetosheath jets occur mainly in the quasi-parallel magnetosheath (Plaschke et al., 2013; Archer and Horbury, 2013; Vuorinen et al., 2019), and they form particularly frequently and travel deeper into the magnetosheath when the angle between the IMF direction and the Sun-Earth line – the cone angle – is small, the solar wind Alfvén Mach number is high, and the solar wind density is low (LaMoury et al., 2021; Koller et al., 2023). The dynamic pressure enhancements of jets may be associated with either increased density, increased velocity, or both (e.g. Archer and Horbury, 2013). Jets are also usually associated with enhanced magnetic field strength (especially when the density is enhanced, see Plaschke et al., 2013; Archer and Horbury, 2013; Karlsson et al., 2015) and decreased plasma temperature (Archer et al., 2012; Dmitriev and Suvorova, 2012; Plaschke et al., 2013). Jets have typical spatial scales of 1 R_E, but studies of jet morphology have found that the shapes and sizes of jets can vary quite significantly (see Plaschke et al., 2018). Jets whose propagation velocities are more aligned with the Sun-Earth line than the ambient magnetosheath flow velocity is, or form very close to the subsolar point and are advected by the magnetosheath flow, can reach the magnetopause. These jets have been found to be quite common, with magnetopause impacts being estimated to occur several times per hour (Plaschke et al., 2016). Jets impacting the magnetopause can have effects on the magnetosphere by e.g. launching magnetospheric ULF waves (Archer et al., 2013; Wang et al., 2022), causing reconnection at the magnetopause (Hietala et al., 2018), and enhancing particle precipitation into the ionosphere (Hietala et al., 2012).

Many different mechanisms for the formation of magnetosheath jets have been suggested. Hietala et al. (2009, 2012) proposed that ripples on the bow shock surface can allow solar wind plasma to traverse the shock with only minimal deceleration, while Archer et al. (2012) suggested that solar wind discontinuities passing through the bow shock could lead to dynamic pressure enhancement. According to Savin et al. (2012), hot flow anomalies (HFAs) at the shock could generate jets. Karlsson et al. (2015) proposed that foreshock short, large-amplitude magnetic structures (SLAMS) impacting the shock could travel through the shock and become jets. Investigating the formation mechanism of a jet with spacecraft measurements is challenging, as observing jet formation requires very fortuitous conjunctions of multiple spacecraft (as in e.g. Raptis et al., 2022a). Numerical simulations do not have this limitation (though they have others) and are thus useful in investigating jet formation mechanisms. E.g. Omelchenko et al. (2021) used the 3D hybrid-PIC simulation HYPERS to formulate a theory that turbulent entanglement of solar wind and magnetospheric magnetic field lines can provide favourable conditions for incursion of fast solar wind plasma into the magnetosheath and the formation of magnetosheath jets.

In Suni et al. (2021), we investigated the formation of jets by conducting a statistical study of jets and foreshock compressive structures (FCS) – defined as structures of enhanced dynamic pressure and magnetic field strength in the foreshock – in four simulation runs performed with the Vlasiator global hybrid-kinetic plasma simulation. We found that 75% of magnetosheath jets form in association with an FCS impacting the bow shock, and that these "FCS-jets" travel farther from the bow shock into the magnetosheath than the remaining 25% of jets. In this study, we analyse the plasma and magnetic field properties at and around the formation time and location of simulated jets that were not associated with FCSs (non-FCS-jets) in Suni et al.

(2021). Because the direction of propagation is important for the potential geoeffectiveness of jets, we classify the non-FCS-jets based on propagation direction and then study the properties of, and differences between, the different categories of jets through case studies and statistical analysis. We also perform the statistical analysis for FCS-jets as a comparison.

2 Model and methods

2.1 Vlasiator

Vlasiator (Palmroth et al., 2018a) is a global magnetospheric, high performance hybrid-Vlasov simulation. It models protons as velocity distribution functions and electrons as a massless charge-neutralising fluid. The proton distribution functions evolve in time according to the Vlasov equation, while the electromagnetic fields evolve according to Maxwell's equations and Ohm's law including the Hall term. Vlasiator is intrinsically 6-dimensional (6D), with 3 position space dimensions (x,y,z) and 3 velocity space dimensions (v_x, v_y, v_z).

In this study we investigate four Vlasiator simulation runs (see simulation parameters in Table 1). These runs are the same ones studied by Palmroth et al. (2021) and Suni et al. (2021), and they neglect the position space z-dimension in order to limit the computational costs of the simulation. The four runs thus simulate the Geocentric Solar Ecliptic (GSE) xy-plane, with simulation boxes large enough to capture the solar wind, foreshock, dayside magnetosheath and magnetosphere, and partially the nightside. Figure 1a) shows the dynamic pressure in the entire simulation domain in run HM05 at an example time $t = 489.5$ s. The IMF is quasi-radial ($< 45°$ IMF cone angle) in all runs. The outer simulation boundaries are periodic in the out-of-plane ($\pm z$) directions, the $\pm y$ and $-x$ boundaries apply homogeneous Neumann conditions, and the $+x$ boundary is set according to the constant solar wind parameters. In all four runs the inner simulation boundary consists of a perfect conductor at a radius of 5 R_E from the origin, which is at the center of the Earth. The high solar wind velocity was chosen to facilitate quick development of the bow shock and magnetosheath in the simulation. The Alfvén Mach number, which is the most important parameter for realistic evolution of the plasma environment near Earth's bow shock, is however within the normal range of observations at Earth in all the runs (Winterhalter and Kivelson, 1988; Ma et al., 2020).

2.2 Jet identification and tracking

In order to identify, separate and track magnetosheath jets over time, we use the methods developed in Palmroth et al. (2021) and Suni et al. (2021). We search for jets in a search box which is chosen to focus on the subsolar magnetosheath in each run and for a tracking duration, limited by the simulation duration of each run, starting at 290 s (see Table 1). The extents of the search box in run HM05 are marked with black dotted lines in Fig. 1a. We define jets according to the criterion presented in Archer and Horbury (2013) as regions consisting of cells in the magnetosheath where the instantaneous dynamic pressure is at least twice the 3-minute moving time average of the dynamic pressure, $P_\mathrm{dyn} \geq 2\langle P_\mathrm{dyn}\rangle_\mathrm{3min}$. Due to the limited simulation durations of the runs used in this study, we use a 3-minute time average instead of the original 20-minute time average used by Archer and Horbury (2013). The regions fulfilling this criterion at one time step in run HM05 are delineated with green

Table 1. Parameters of the different simulation runs used in the study. From left to right, the columns give the run identifier, IMF vector in GSE, IMF strength, IMF cone angle, solar wind number density, solar wind velocity, solar wind Alfvén Mach number, box in which jets were searched for ($x_{\min}$,$x_{\max}$,$y_{\min}$,$y_{\max}$), and jet tracking duration. For all runs, the solar wind temperature is 0.5 MK, the position space resolution is 227 km, and the velocity space resolution is 30 kms^{-1}.

Run	$\boldsymbol{B}_{\mathrm{IMF}}$ [nT]	$\lvert\boldsymbol{B}_{\mathrm{IMF}}\rvert$ [nT]	Cone angle [°]	n [cm^{-3}]	v_x [kms^{-1}]	M_{A}	Search box [R_{E}]	Tracking duration [s]
HM30	(–4.3, 2.5, 0)	5	30	1	–750	6.9	(6, 18, –8, 6)	129.5
HM05	(–5.0, 0.4, 0)	5	5	3.3	–600	10	(6, 18, –6, 6)	299.5
LM30	(–8.7, 5.0, 0)	10	30	1	–750	3.4	(6, 18, –8, 6)	379.5
LM05	(–10.0, 0.9, 0)	10	5	3.3	–600	5	(6, 18, –6, 6)	149.5

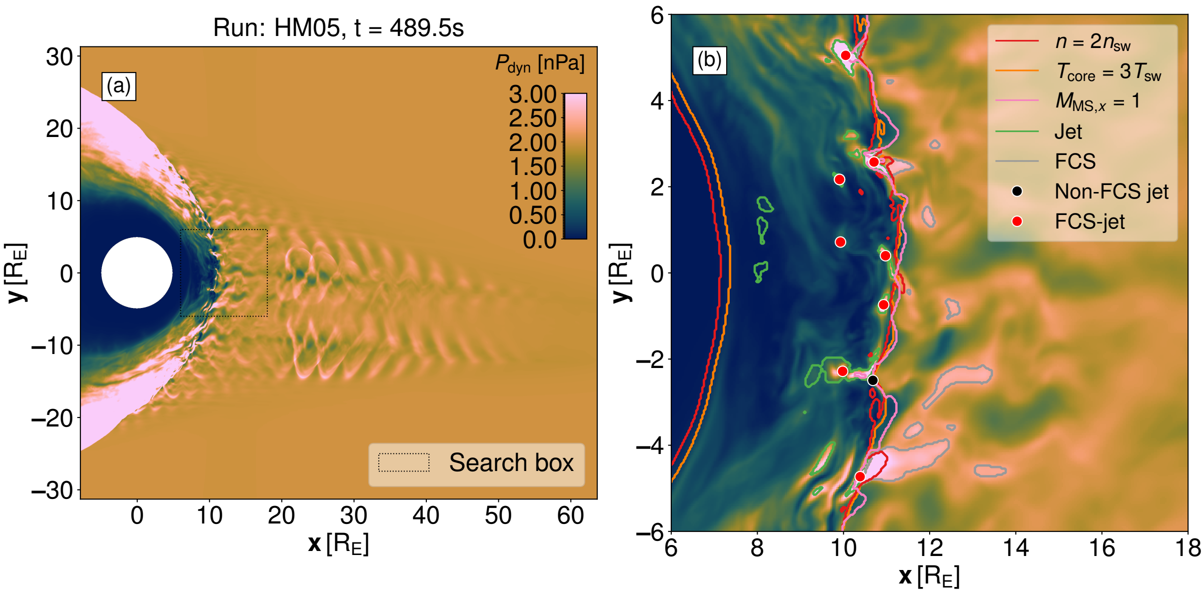

Figure 1. (a) Overview of dynamic pressure in the entire simulation box of run HM05 at an example time $t = 489.5$s. The dotted black box shows the extents of where we search for jets in this run. (b) Zoomed-in view of the search box at the same time in the same run. The plasma compression, plasma heating, and magnetosonic Mach number bow shock criteria are plotted as red, orange, and pink contours, respectively. Jets and FCSs are delineated by green and grey contours, respectively. Non-FCS-jets and FCS-jets are marked with black and red dots, respectively.

contours in Fig. 1b. Jets that are identified at only one time step are discarded, as their propagation cannot be calculated from tracking the jet. While the method we use can identify jets anywhere in the magnetosheath, we additionally require that the jets we study form at the bow shock, as Palmroth et al. (2021) proposed that regions fulfilling the jet criteria that form deeper in the

https://doi.org/10.5194/angeo-2023-14
Preprint. Discussion started: 11 May 2023

magnetosheath are merely momentary dynamic pressure fluctuations in a low ambient dynamic pressure environment rather than jets. We define the bow shock in three different ways adapted from Battarbee et al. (2020): The boundary where the ion density is twice the solar wind density, $n = 2n_{\mathrm{sw}}$ (plasma compression); the boundary where the temperature of the core ion population (as discussed in Wilson et al., 2014) is 3 times the solar wind temperature, $T_{\mathrm{core}} = 3T_{\mathrm{sw}}$ (plasma heating); and the boundary where the x-directional magnetosonic Mach number is 1, $M_{\mathrm{ms},x} = 1$ (red, orange, and pink contours, respectively, in Fig. 1). The magnetosheath is defined using the temperature criterion as the region of the simulation where $T_{\mathrm{core}} \geq 3T_{\mathrm{sw}}$. A jet is considered to form at the bow shock if the position space simulation cells comprising the jet are in contact with either the temperature boundary or the Mach number boundary. The density boundary is not used for this purpose as it constantly fluctuates at the quasi-parallel shock due to shock reformation (Schwartz and Burgess, 1991; Johlander et al., 2022). The x-directional Mach number is a suitable proxy for the bow shock location only near the nose of the bow shock, but as we search for jets in a subregion of the dayside magnetosheath (see Table 1), the behaviour of the x-directional Mach number at the flanks is not an issue.

The jets that form at the bow shock are initially separated into two categories as in Suni et al. (2021): Those that form in contact with FCSs, called FCS-jets (marked with red dots in Fig. 1b); and those that do not, which are called non-FCS-jets (marked with a black dot in Fig. 1b). In Suni et al. (2021) we defined FCS as structures in the foreshock where the dynamic pressure is at least 1.2 times the solar wind dynamic pressure and the magnetic field strength is at least η times the interplanetary magnetic field strength,

$$\begin{aligned} P_{\mathrm{dyn}} &\geq 1.2 P_{\mathrm{dyn,sw}} \\ |\boldsymbol{B}| &\geq \eta |\boldsymbol{B}_{\mathrm{IMF}}|, \end{aligned} \tag{1}$$

where η is a threshold that can take values between 1.1 and 3.0. In order to capture even the weakest FCS, in this study we use $\eta = 1.1$. The regions fulfilling the FCS criteria are delineated with grey contours in Fig. 1b).

3 Results

3.1 Jet Classification

In order to study the propagation of jets in the magnetosheath, we define for each jet

- a formation time t_0
- a formation site (x_0, y_0),

where t_0 is the earliest simulation time step at which the jet is identified and, to emphasise the parts of the jet with higher dynamic pressure, (x_0, y_0) is a weighted mean of the cells comprising the jet,

$$(\bar{x}, \bar{y})(t) = \left(\frac{\sum\limits_{k \in cells(t)} w_k x_k}{\sum\limits_{k \in cells(t)} w_k}, \frac{\sum\limits_{k \in cells(t)} w_k y_k}{\sum\limits_{k \in cells(t)} w_k} \right), \quad w_k = \frac{P_{\mathrm{dyn},k}}{\langle P_{\mathrm{dyn},k} \rangle_{3\mathrm{min}}} - 2, \tag{2}$$

https://doi.org/10.5194/angeo-2023-14
Preprint. Discussion started: 11 May 2023

at t_0, $(x_0, y_0) = (\bar{x}, \bar{y})(t_0)$, where the weights w_k are a measure of how much the dynamic pressure of each cell exceeds the criterion used to define the jets. To calculate the propagation velocity of the dynamic pressure enhancement associated with the jet, we define a formation of three virtual spacecraft (VSC) in an equilateral triangle centered on (x_0, y_0) and with an inter-spacecraft separation of $\sqrt{3}dx$, where $dx = 227$ km is the position space resolution (cell size) of the simulation runs (see Table 1 caption), which gives $\sqrt{3}dx \approx 393$ km $\approx 0.06\ R_\mathrm{E}$ (see Fig 2a). Assuming that the propagating structure can be considered a plane wave, we apply multi-spacecraft timing analysis (Paschmann and Daly, 1998; Schwartz, 1998) to the time series of dynamic pressure measured from $t_0 - 10$ s to $t_0 + 10$ s at each of the three VSCs. This yields the propagation velocity $\boldsymbol{v_n}$ along the normal direction $\hat{\boldsymbol{n}}$ of the dynamic pressure enhancement corresponding to the jet. We estimate the propagation velocity in the spacecraft frame $\boldsymbol{v_\mathrm{SC}}$ of the jet as $\boldsymbol{v_\mathrm{SC}} = \boldsymbol{v_\mathrm{bulk}} + (v_n - \boldsymbol{v_\mathrm{bulk}} \cdot \hat{\boldsymbol{n}})\hat{\boldsymbol{n}}$ (similarly as in Archer et al., 2005), where $\boldsymbol{v_\mathrm{bulk}}$ is the mean bulk velocity measured by a reference spacecraft, for which the VSC at $(x_0, y_0 + dx)$ was chosen, in the $[t_0 - 10\ \mathrm{s},\ t_0 + 10\ \mathrm{s}]$ interval. Subintervals where the VSC is considered to be in the foreshock (defined as $T_\mathrm{core} < 3T_\mathrm{sw}$), if any, are excluded.

For each jet, we also use the time-evolution of $(\bar{x}, \bar{y})$ to calculate an alternative propagation velocity $\boldsymbol{v_\mathrm{tr}}$, defined by the change of $(\bar{x}, \bar{y})$ from t_0 to t_1:

$$\boldsymbol{v_{tr}} = \frac{(\bar{x}, \bar{y})(t_1) - (\bar{x}, \bar{y})(t_0)}{t_1 - t_0}, \tag{3}$$

where t_1 is taken 2 seconds (4 output time steps at 0.5 s time resolution) after jet formation. If the jet only exists for less than 2 seconds, then t_1 is the last time when the jet is identified.

Analysing the propagation velocities of non-FCS-jets, we find that they can be classified based on whether they propagate antisunward or toward the flanks. We classify the non-FCS-jets according to their directions of propagation in the spacecraft frame $\boldsymbol{v_\mathrm{SC}}$: Jets whose propagation velocity vector is within $45°$ from the antisunward $(-x)$ direction are classified as "antisunward jets", while the remaining jets are classified as "flankward jets". In cases when the maximum cross-correlation of the dynamic pressure time series between any VSC pair is less than 0.8 (Eastwood et al., 2005a), we deem the timing analysis possibly unreliable and perform the classification based on $\boldsymbol{v_\mathrm{tr}}$ instead. After the non-FCS-jets are categorised in this way, the formation sites and times of the jets are visually inspected and jets that are not actually connected with the bow shock (as defined by the core heating or magnetosonic Mach number criteria) or which are clearly part of the same structure as any previously identified jet are discarded. Table 2 shows the number of jets of each category found in each of the four simulation runs, as well as the number of FCS-jets for comparison and the ratios of the numbers of antisunward, flankward, total non-FCS-jets, and FCS-jets to the total number of all jets. FCS-jets make up 71% of all jets, which is in agreement with the results of Suni et al. (2021). Non-FCS-jets make up the remaining 29% of jets, and roughly half of the non-FCS-jets are antisunward and half flankward. The ratio of antisunward jets to flankward jets is > 1 for the 5° IMF cone angle runs, and < 1 for the 30° cone angle runs.

Figure 2b)-d) shows the propagation velocities $\boldsymbol{v_\mathrm{SC}}$ and $\boldsymbol{v_\mathrm{tr}}$ for all flankward jets, antisunward jets, and FCS-jets respectively, as well as the medians of the propagation velocities and average bulk velocity at the reference VSC, with the median Alfvén and magnetosonic speeds at the reference VSC for comparison. Unreliable $\boldsymbol{v_\mathrm{SC}}$ are not plotted or included in median

https://doi.org/10.5194/angeo-2023-14
Preprint. Discussion started: 11 May 2023

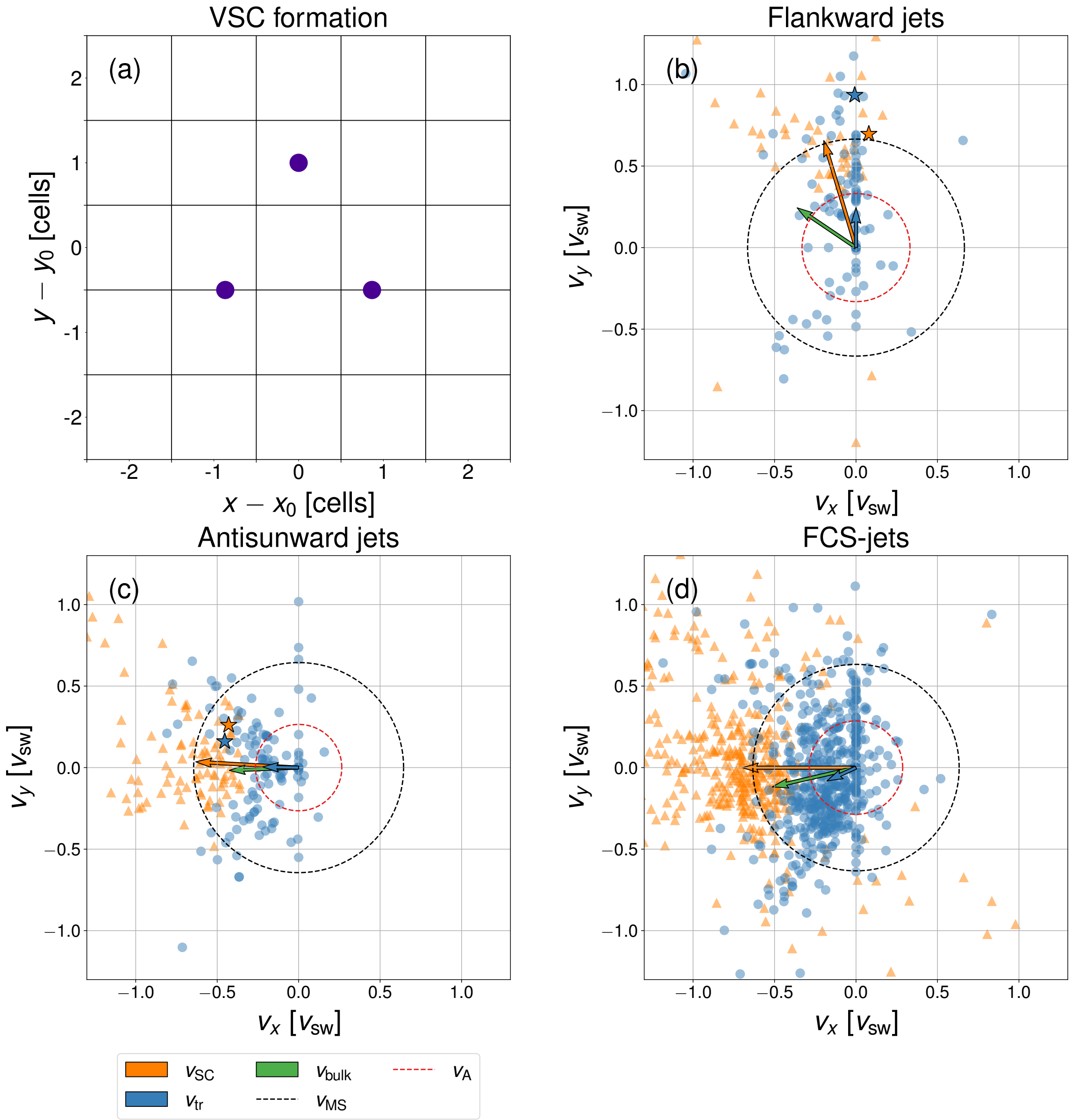

Figure 2. (a) Virtual spacecraft triangle formation, with respect to formation site (x_0, y_0), used in the timing analysis. (b-d) Jet propagation velocities in the spacecraft frame calculated from timing analysis (orange triangles) and based on the tracking of the weighted centers of the jets (blue dots), as well as median bulk velocity (green arrow) and median Alfvén (red circle) and magnetosonic speeds (black circle) for (b) flankward jets, (c) antisunward jets, and (d) FCS-jets. Individual markers show the propagation velocity vectors of individual jets while the arrows show the medians of each velocity. The stars mark the propagation velocities of example jets used in the case studies. Jet propagation velocities from timing analysis for which the maximum cross-correlation between any VSC pair is less than 0.8 are deemed unreliable and are not plotted or included in the calculations of the medians.

Table 2. Number of jets of each category and total number of non-FCS-jets found in each of the different simulation runs as well as in all runs combined. The number of FCS-jets found in each run and all runs combined are also given, as well as the proportions of the different jet categories and FCS-jets to the total number of jets.

Run	Antisunward jets	Flankward jets	Total non-FCS-jets	FCS-jets	All jets
HM30	8	22	30	61	91
HM05	31	15	46	145	191
LM30	37	59	96	251	347
LM05	44	13	57	105	162
All	120	109	229	562	791
% of all jets	15	14	29	71	100

calculations. The v_x- and v_y-axes are both cropped to $[-1.3v_{\mathrm{sw}},\ 1.3v_{\mathrm{sw}}]$ as this allows the majority of the data points to be shown without obscuring the medians and Alfvén and magnetosonic speeds. 6 flankward jet, 8 antisunward jet, and 58 FCS-jet $\boldsymbol{v}_{\mathbf{SC}}$ data points fall outside the axes limits, while 0, 1, and 20 flankward, antisunward and FCS-jet $\boldsymbol{v}_{\mathbf{tr}}$ data point fall outside the axes. We can see that in the case of flankward jets, propagation is biased toward the dusk flank, as is the bulk flow, which suggests that most flankward jets form on the duskward side of the subsolar point. For antisunward jets and FCS-jets, on the other hand, the propagation velocities and bulk flow are distributed almost equally on the dawn and dusk sides, while the bulk flow is slightly biased toward dawn for FCS-jets. This is consistent with the deflection of the antisunward solar wind flow by the shock around the subsolar point. Most flankward jets propagate faster flankward than the bulk flow, while the propagation of antisunward jets appears to be quite closely aligned with the bulk flow. For all jet types, we can see some cases where $\boldsymbol{v}_{\mathbf{tr}}$ has no x-directional component. This is likely due to those particular jets being very short-lived and extending only one cell in the x-direction, in which case the weighted center coordinate is effectively quantised due to the finite simulation cell size.

3.2 Case studies

Having classified the non-FCS-jets, we investigate possible differences in the plasma and magnetic field properties surrounding the formation of jets of different categories by selecting one typical flankward jet (marked with stars in Fig. 2b) and one typical antisunward jet (marked with stars in Fig. 2c) as examples for individual analysis. Figure 3 shows the properties surrounding the formation of the example flankward jet: Panel a) shows the dynamic pressure around the formation site (marked by the crosshairs) at t_0, with contours delineating regions where the different bow shock criteria and the jet and FCS criteria are fulfilled. The black dot marks the weighted center $(\bar{x}, \bar{y})$ of the flankward jet in question. The streamlines show the magnetic field. Panel b) shows the time series from $t_0 - 10$ s to $t_0 + 10$ s of dynamic pressure along a line segment centered on (x_0, y_0) and extending 20 cells ($\sim 0.71\ R_{\mathrm{E}}$) in the $-x$ and $+x$ directions. Also shown are contours marking the x-coordinates of the three bow shock criteria at y_0 as a function of time, and crosshairs marking (x_0, t_0). Panel c) shows the results of the timing analysis for the flankward jet under consideration. Panels d)-h) show the time series from $t_0 - 10$ s to $t_0 + 10$ s at the formation site of density; velocity x-component, magnitude of the yz-components and the total magnitude; dynamic pressure; magnitude of the magnetic field x-component, yz-components and the total field; and temperature components perpendicular and parallel to the magnetic field. The decision to show yz-components instead of y and z separately was made to highlight the difference between the antisunward component and its orthogonal counterpart, as the magnetosheath flow and the effect of IMF clock angle on the magnetosheath are expected to be roughly rotationally symmetric. To improve clarity, we plot $|B_x|$ instead of B_x. as the sign of B_x is mainly determined by the sign of the IMF B_x. The dashed lines mark t_0.

We can see from the simulation view (Fig. 3a) that the jet forms at the bow shock several R_E duskward of the subsolar point, and that while waves are visible in the magnetic field on the upstream side, the dynamic pressure sunward of the jet is quite homogeneous, indicating the absence of compressional waves. This suggests that the formation site is close to the ULF foreshock edge. Immediately sunward of the formation site, the three bow shock criteria are not exactly co-located – the magnetosonic Mach boundary is sunward of the other two – i.e. the bow shock is “non-local” (Battarbee et al., 2020). The cut-through time series shows that the formation of the jet is associated with lower dynamic pressure upstream of the formation site. Just before the formation time, the appearance of the bow shock non-locality can be seen. Fig. 3c) shows that the magnetosheath bulk velocity is sub-Alfvénic, while the jet propagation velocities are all super-Alfvénic in the spacecraft frame. The weighted center of the jet even propagates with supermagnetosonic speed. The time series show that the formation of the jet is associated with a large and steep increase in plasma density, as well as deflection of the plasma flow from v_x-dominated to v_{yz}-dominated. The formation is also preceded by a strengthening of B_x and weakening of B_{yz}. Just before the formation time, there is a large increase in $T_\perp$ and a small decrease in $T_\parallel$, and as a consequence the temperature anisotropy $T_\perp/T_\parallel$ increases.

Figure 4 shows the surroundings of the forming example antisunward jet, presented in the same way as the example of the flankward jet. The simulation view in panel a) shows that this antisunward jet also forms several R_E duskward of the subsolar point, but under very different conditions. As the simulation run in question has an IMF cone angle of $5°$, the formation site is downstream of the deep ULF foreshock. The magnetic field both upstream and downstream is highly wavy, and compressional structures can be seen on the upstream side. The bow shock immediately sunward of this jet is also non-local, but now the magnetosonic Mach number boundary is earthward of the other two bow shock boundaries. In the cut-through time series, we can see a foreshock dynamic pressure enhancement advecting toward and impacting the bow shock, which is followed by the formation of the jet at the impact location. A few seconds after the formation time, a bow shock reformation event (see Johlander et al., 2022) occurs, as shown by the red contour extending further into the upstream in Fig. 4b). The timing analysis shows that the jet propagation velocities and ambient bulk velocity are all super-Alfvénic but submagnetosonic, and the jet propagates in the bulk flow direction. The time series show that the formation of the jet is associated with an increase in density and magnetic field strength, to which the B_{yz} component contributes more than B_x. The formation is preceded by enhanced v_x and a decrease in v_{yz} as well as a decrease in both $T_\perp$ and $T_\parallel$ and approximately isotropic temperature.

3.3 Statistical analysis

The examples show that flankward and antisunward jets appear to differ in the properties of the plasma surrounding and comprising them. To investigate this further, we conduct a statistical study of all flankward, antisunward and FCS-jets. Figure

https://doi.org/10.5194/angeo-2023-14
Preprint. Discussion started: 11 May 2023

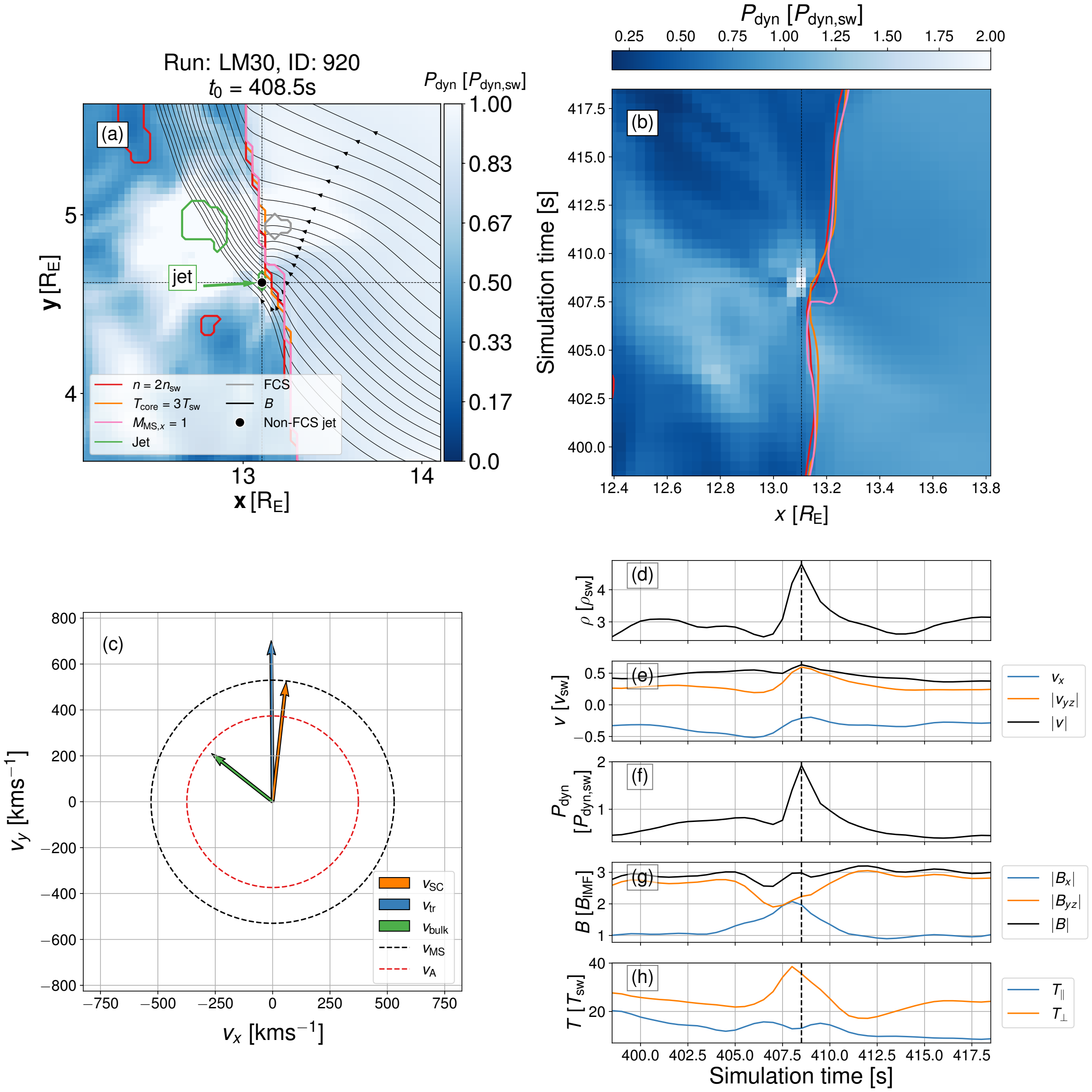

Figure 3. Properties of the near-bow shock environment around the formation time t_0 and place (x_0, y_0) of an example flankward jet: (a) view of dynamic pressure with contours showing the fulfilling of the three bow shock criteria (plasma compression in red, plasma heating in orange, and magnetosonic Mach number in pink), the jet criteria (green), and FCS criteria (grey), with black dots indicating the weighted centers of tracked non-FCS-jets, and magnetic field lines shown as black streamlines; (b) cut-through time series around t_0 and x_0 at y_0 showing dynamic pressure and the three bow shock criteria as contours; (c) timing analysis from a triangle of VSCs centered on (x_0, y_0), showing propagation velocities, bulk velocity, and Alfvén and magnetosonic speeds; (d-h) time series of plasma and magnetic field properties around t_0 at (x_0, y_0).

https://doi.org/10.5194/angeo-2023-14
Preprint. Discussion started: 11 May 2023

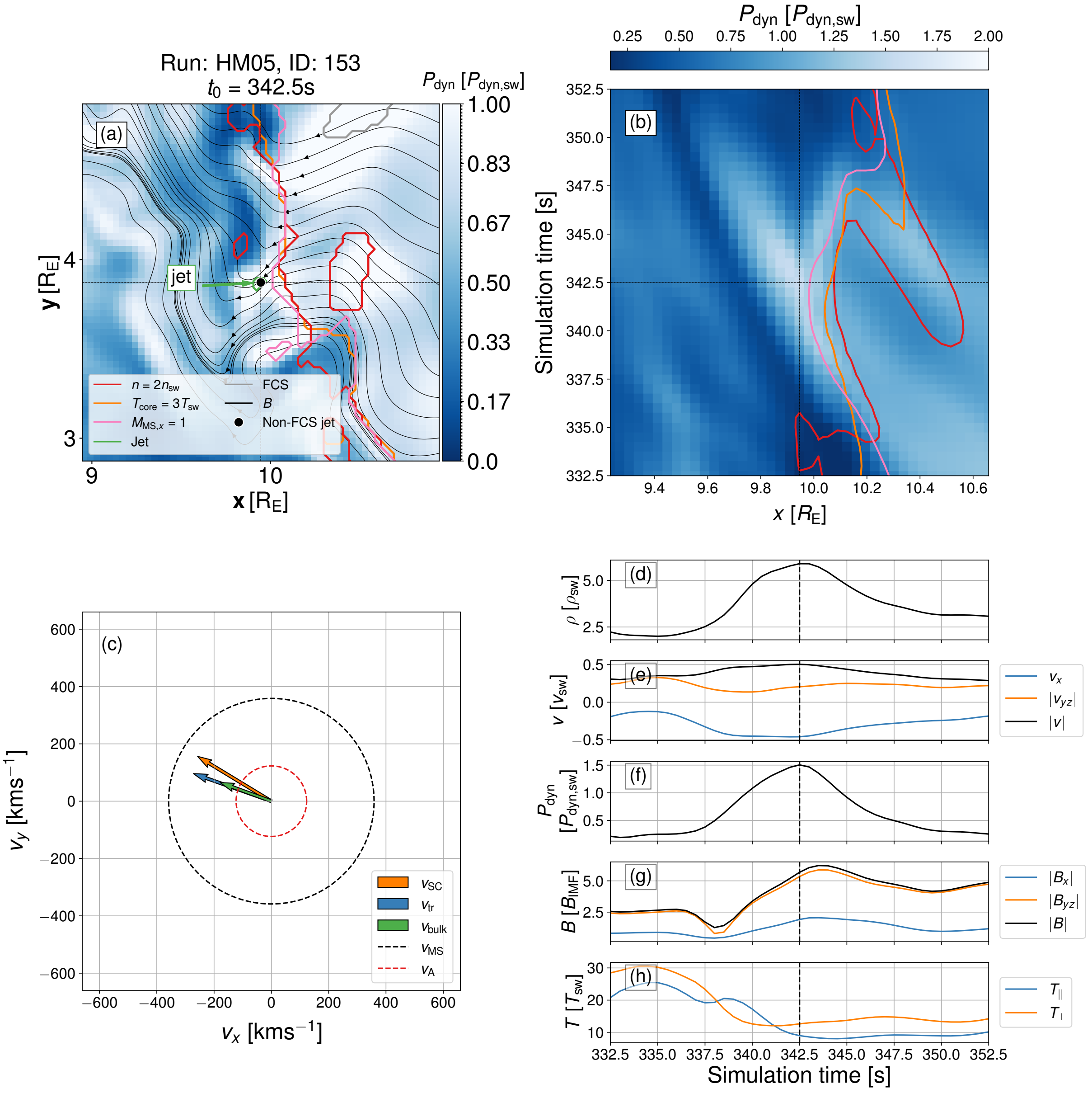

Figure 4. Same format as Figure 3 for an example antisunward jet.

https://doi.org/10.5194/angeo-2023-14
Preprint. Discussion started: 11 May 2023

5 shows a superposed epoch analysis (SEA) of cut-through time series of plasma density (panels a, f, k), v_x (panels b, g, l), dynamic pressure (panels c, h, m), magnetic field strength (panels d, i, n), and temperature (panels e, j, o), with t_0 of each jet serving as the epoch time and x_0 serving as the epoch x. Also shown are the average bow shock distances at y_0 as a function of time. We can see that on average, flankward jets are not associated with any foreshock structures convecting into the bow shock, at least not exactly sunward of the formation sites. Flankward jets also appear to be mainly density-driven, with little to no velocity enhancement in the magnetosheath at the formation site and time, but a noticeable enhancement of density. The plasma at the formation site and time is generally cooler than the ambient magnetosheath plasma but is surrounded by localised temperature enhancements. Flankward jets are associated with a sunward motion of the bow shock, with the motion becoming faster after the formation time. The jet formation is also followed by an enhancement of magnetic field strength in the magnetosheath. Antisunward and FCS-jets, on the other hand, appear to be very similar to each other and different from flankward jets. Both are associated with foreshock structures of enhanced density, dynamic pressure, and magnetic field advecting into the bow shock. The impact is concurrent with jet formation and the incursion of fast and cold solar wind plasma into the magnetosheath.

Figure 6 shows a SEA of the time series at the jet formation sites of plasma density (panels a, g, m), velocity components and magnitude (panels b, h, n), dynamic pressure (panels c, i, o), magnitude of magnetic field components and total field (panels d, j, p), parallel and perpendicular temperature (panels e, k, q), and temperature anisotropy (panels f, l, r) for flankward jets, antisunward jets, and FCS-jets. The formation time of each jet is chosen as the epoch time. Also shown are box-and-whisker plots showing the median, 25th percentile, 75th percentile, and the lowest and highest data points that are within 1.5 times the interquartile range (IQR) from the quartiles of the time series data used in the SEA sampled at epoch times -6.5 s, 0 s, and 6.5 s. We can see that flankward jets exhibit the greatest density enhancement on average, while FCS-jets exhibit the smallest. To some extent, this may be affected by the fact that most jets of all kinds are found in runs LM05 and LM30 (see Table 2), where the low solar wind Alfvén Mach number may lead to less compression of the plasma at the shock. In contrast, FCS-jets display the greatest enhancement in velocity, while flankward jets display the smallest. For flankward jets the velocity enhancement is in the v_{yz}-component, unlike for antisunward and FCS-jets where both v_x and v_{yz} are enhanced. The resulting enhancement in dynamic pressure is similar for all kinds of jets. The magnetic field enhancement is also similar across all categories, with the main difference being an enhancement in B_{yz} after jet formation for flankward jets. The formation of all kinds of jets is preceded by and associated with a decrease in $T_{\parallel}$, but for flankward jets formation is associated with nearly constant $T_{\perp}$ that leads to enhanced temperature anisotropy, whereas for antisunward and FCS-jets $T_{\perp}$ also decreases around the formation time. The box-and-whisker plots show that there is considerable variation in the time series of jets belonging to each category, but the interquartile ranges are similar to the differences between the categories.

Finally, we investigate the formation sites of the different jet categories. Figure 7 shows the formation sites of flankward jets and antisunward jets, as well as FCS-jets for comparison, in the four simulation runs. Also depicted are the extent of the ion foreshock, defined as the presence of reflected ions (black dashed curve visible in panels b and d), the extent of the ULF foreshock, defined as enhancement of B_z, at $t = 400$ s in each run, similarly as in Turc et al. (2018) (pink and brown contours), and the extent of the jet search box (black dotted lines, see Table 1) in each run. The example jets studied in section

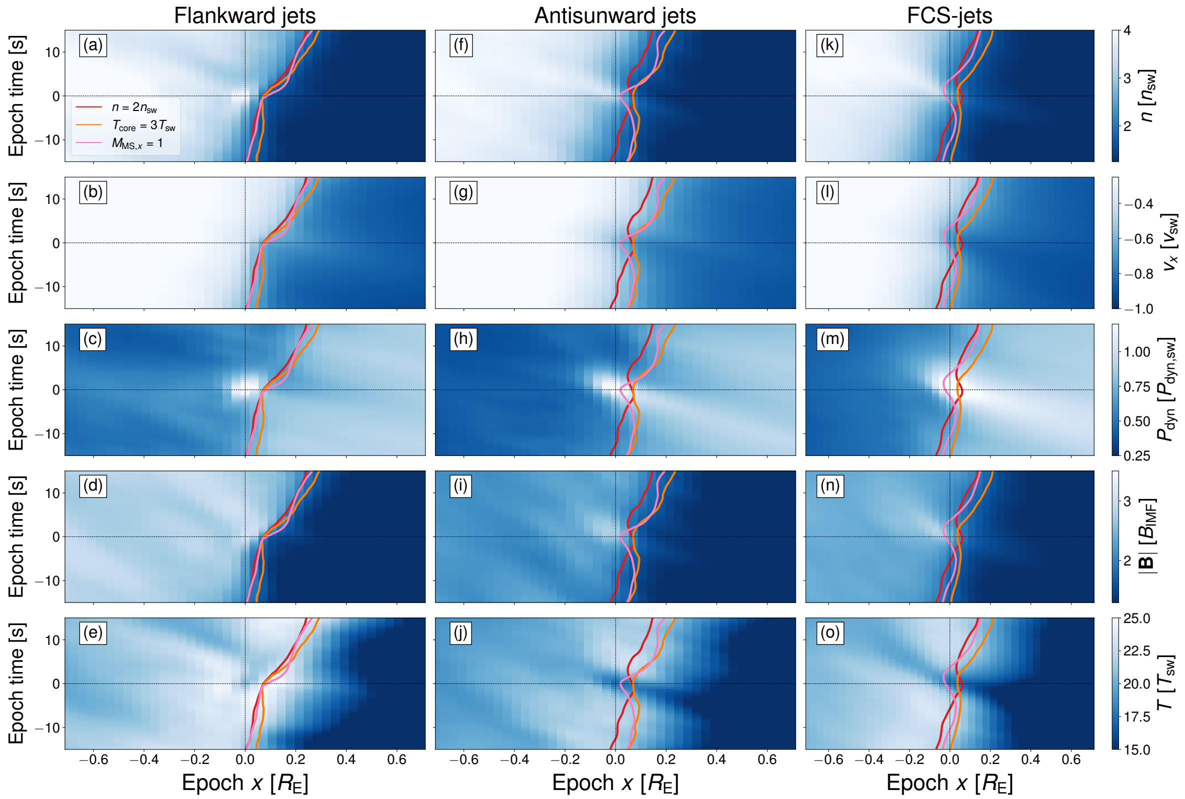

Figure 5. Superposed epoch analysis of cut-through time series of plasma density, x-directional velocity component, dynamic pressure, magnetic field strength, and temperature for flankward jets, antisunward jets, and FCS-jets. The formation time t_0 for each jet was chosen as the epoch time, while the formation site x-coordinate x_0 was chosen as the epoch location. Also shown are the average locations of the plasma density, plasma heating, and magnetosonic Mach number bow shock criteria as red, orange, and pink contours, respectively.

3.2 are marked with stars. We can see that antisunward and FCS-jets form everywhere at the bow shock in the search box in all simulation runs, but the majority of flankward jets form at the edge of the ULF foreshock on the dusk flank side, in agreement with the median bulk velocity in Fig. 2b, in the 30° IMF cone angle runs.

4 Discussion

In this study we have investigated the formation of jets that were not associated with foreshock compressive structures in Suni et al. (2021) by classifying them based on their direction of propagation. We have found that these non-FCS-jets can be separated into two categories: Flankward and antisunward jets, named for their respective propagation directions. We have conducted case studies by analysing two example jets in four different ways: 2D simulation views, cut-through time series, analysis of jet propagation, and virtual spacecraft time series at the formation site. We have performed a statistical analysis

https://doi.org/10.5194/angeo-2023-14
Preprint. Discussion started: 11 May 2023

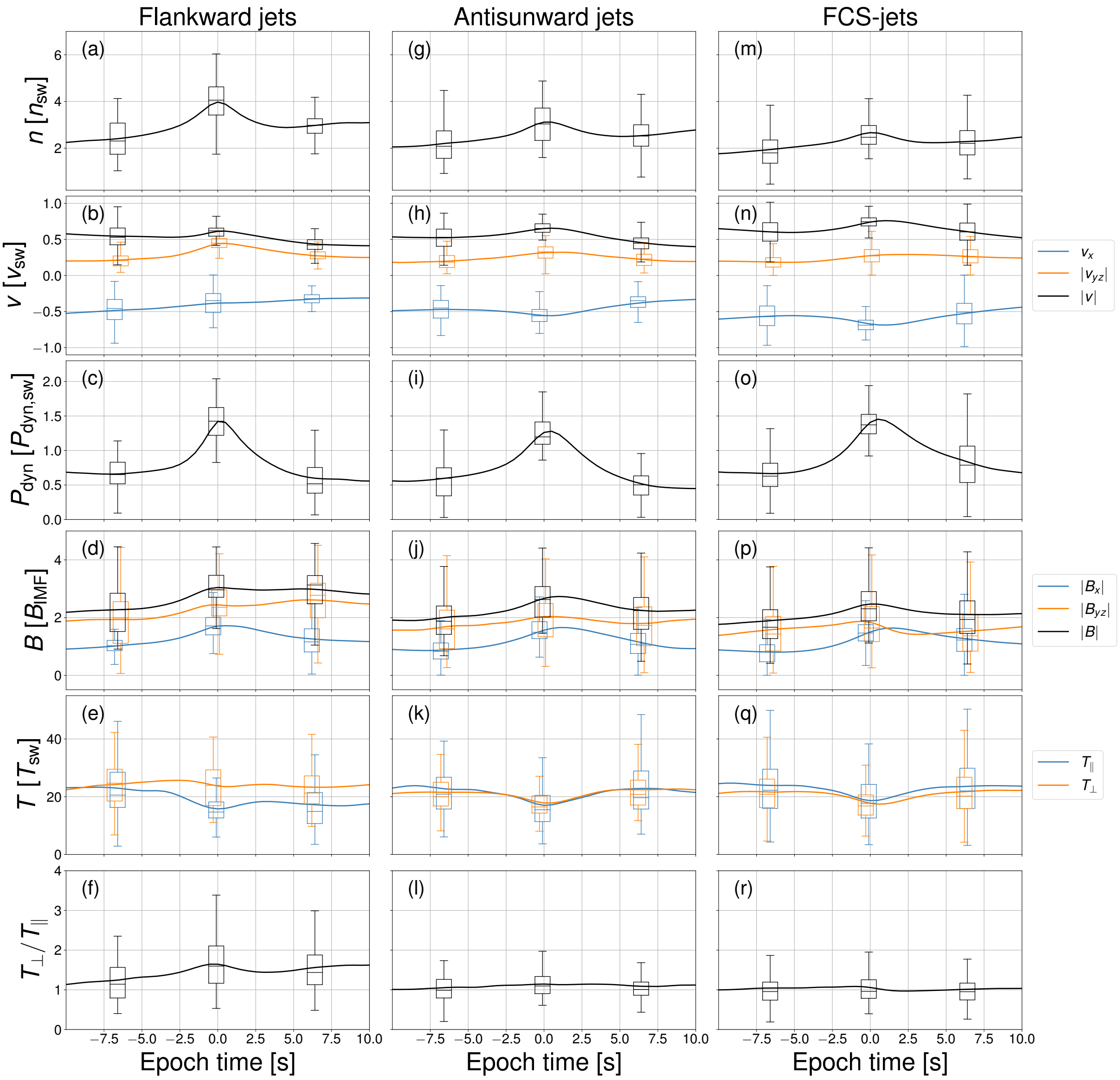

Figure 6. Superposed epoch analysis of single VSC time series, showing density, velocity components and magnitude, dynamic pressure, magnetic field components and magnitude, parallel and perpendicular temperature, and temperature anisotropy for flankward jets, antisunward jets, and FCS-jets. The formation time t_0 of each jet was chosen as the epoch time. Also shown are box-and-whisker plots at epoch times -6.5 s, 0 s, and 6.5 s. The boxes show the 25th percentile, the median and the 75th percentile, while the whiskers mark the lowest and highest data points that are within 1.5 times the interquartile range ($IQR = Q3 - Q1$) from the quartiles.

https://doi.org/10.5194/angeo-2023-14
Preprint. Discussion started: 11 May 2023

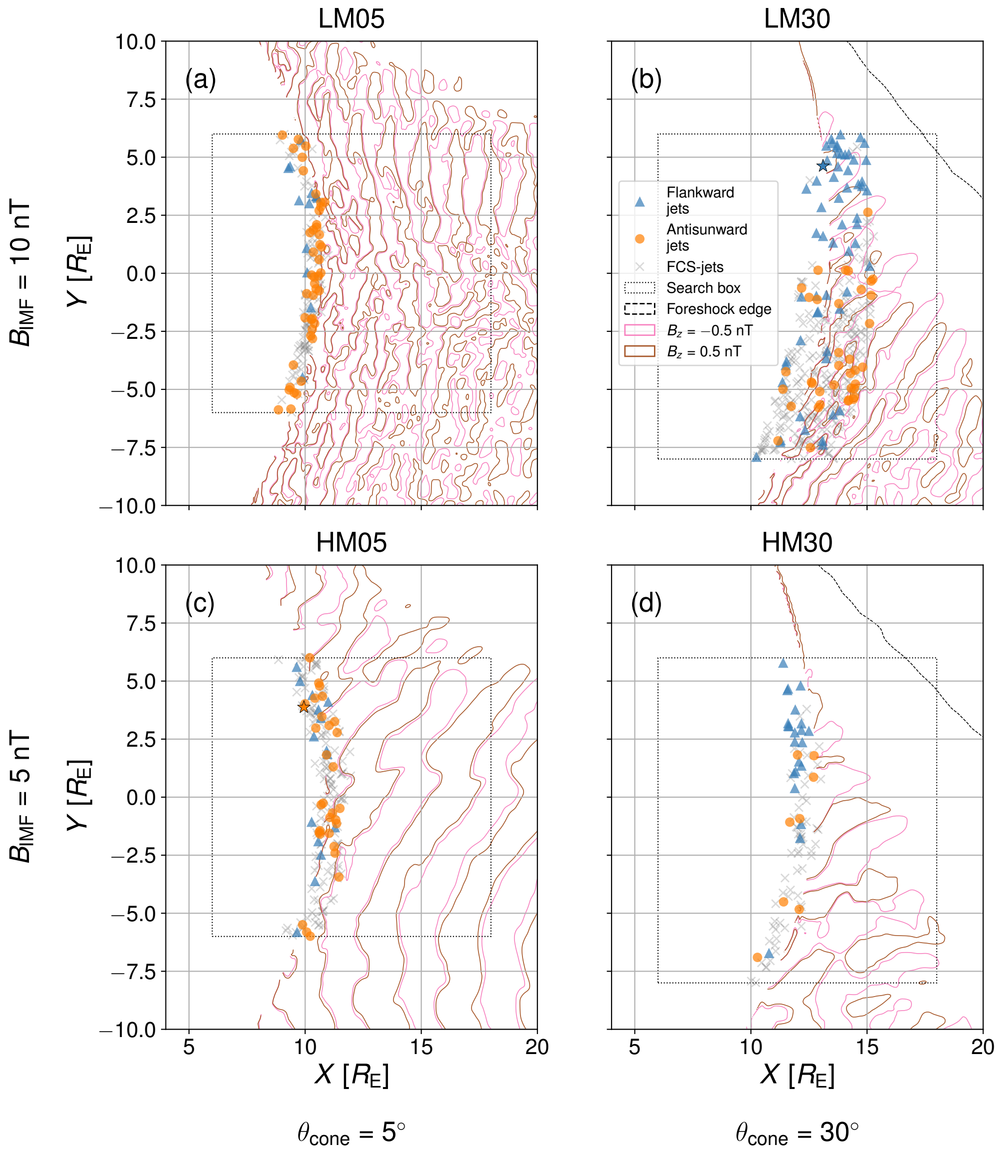

Figure 7. Formation sites (x_0, y_0) of all non-FCS-jets separated by category, as well as FCS-jets for comparison, in the four runs: (a) LM05, (b) LM30, (c) HM05, and (d) HM30. Flankward and antisunward jets are shown as blue triangles and orange circles, respectively. The jets used for the case studies are marked with stars. FCS-jets are shown as grey crosses. The dashed black curve shows the edge of the foreshock, as defined by the presence of reflected ions, and thus the extent of the ion foreshock at $t = 400$ s in each run. The pink and brown curves show, also at $t = 400$ s, the contours of $B_z = -0.5$nT and $B_z = 0.5$nT respectively, indicating the presence of ULF waves and the extent of the ULF foreshock. The horizontal dotted black lines show the extents of the jet search box in each run.

by conducting superposed epoch analyses of the cut-through time series and the virtual spacecraft time series, as well as compared the median propagation velocities and visualised where along the bow shock different jets form, for flankward jets and antisunward jets, as well as FCS-jets for comparison. We have found that antisunward jets strongly resemble FCS-jets in their properties, and that flankward jets differ in many ways from both antisunward and FCS-jets.

As we have seen in Figure 5, antisunward jets resemble FCS-jets in that both are associated with foreshock structures of enhanced density, dynamic pressure and slightly enhanced magnetic field strength convecting into the bow shock, the impact coinciding with jet formation in the magnetosheath. The impact is also associated with the intrusion of fast and cold solar wind plasma into the magnetosheath. We find that the plasma in the jets is colder and faster than the surrounding plasma, which agrees with previous results from Vlasiator and Magnetospheric Multiscale (MMS) spacecraft observations (Palmroth et al., 2021) as well as data from the five Time History of Events and Macroscale Interactions during Substorms (THEMIS) spacecraft (Plaschke et al., 2013). The intrusion of solar wind plasma into the magnetosheath resembles what is expected by the SLAMS theory of jet formation by Karlsson et al. (2015), but here this applies to structures of dynamic pressure and magnetic field enhancement compared to the magnetic field enhancement that defines SLAMS. From Figure 6 we have seen that the velocity enhancement at the jet formation site is mainly in v_x, the magnetic field enhancement is mainly in B_x, and the temperature decrease is both in the parallel and the perpendicular component. Figures 2 and 7 show that antisunward and FCS-jets form in the same regions of the magnetosheath and they both mainly propagate antisunward. Because antisunward and FCS-jets make up 683 of the total 790 jets used in this study (see Table 2), this motivates us to update the result of Suni et al. (2021) and estimate that 86% of jets that form at the bow shock under the steady solar wind conditions and quasi-radial IMF of our four simulation runs are associated with structures of enhanced dynamic pressure and magnetic field strength in the foreshock. This agrees with the formation mechanism proposed by Karlsson et al. (2015).

In contrast, the flankward jets that make up the remaining 14% of the jets investigated in this study have very different properties. Their large temperature anisotropy (with $T_\perp$ being larger than $T_\parallel$, see Figure 6) and the deflection of the shocked solar wind plasma (enhancement of v_{yz} rather than v_x) is reminiscent of the “quasi-perpendicular jets” described by Raptis et al. (2020). However, these quasi-perpendicular jets in Raptis et al. (2020) show modest enhancements or even decreases in the plasma density, while the flankward jets in this study are on average associated with even higher density enhancements than antisunward and FCS-jets. The unexpectedly large overall density found in flankward jets could be due to the 2D nature of the simulation runs used in this study, as this prevents structures from dissipating in the out-of-plane direction (Pfau-Kempf et al., 2016; Suni et al., 2021), though this cannot account for the temporary enhancement in density. From Figure 6 we can also see that the temperature anisotropy at the formation site remains higher than 1 up to 10 seconds after jet formation, as does the enhancement of B_{yz}. This suggests that the formation of flankward jets could be concurrent with a local change in bow shock geometry from quasi-parallel to quasi-perpendicular. Quasi-perpendicular shocks are associated with a sharper jump of plasma and magnetic field properties across the shock than quasi-parallel shocks, which could explain the enhancement of density inside the flankward jets. The enhancement of v_{yz} and decrease in v_x are also consistent with a change in the angle between the bow shock normal and the direction of the incoming solar wind. The local turning of a shock from quasi-parallel to quasi-perpendicular due to growing out-of-coplane magnetic perturbations is a known phenomenon (e.g. Baumjohann and

Treumann, 1996), but this turning has also been observed in association with bow shock reformation (Gingell et al., 2017; Liu et al., 2021). The findings of Liu et al. (2021) that this turning can happen due to reformation at the oblique bow shock could explain why flankward jets form mainly at the edge of the ULF foreshock, which is upstream of the oblique bow shock. At the oblique shock, the ULF waves are able to modulate the upstream conditions but do not generate compressional structures that would lead to the formation of antisunward or FCS-jets instead.

5 Conclusions

In this study we show that 86% of all the jets forming at the bow shock in four Vlasiator simulation runs with steady solar wind conditions and quasi-radial IMF form due to foreshock structures of enhanced dynamic pressure and magnetic field strength impacting the bow shock, consistent with the formation mechanism proposed by Karlsson et al. (2015).

We show that the remaining 14% of jets exhibit different properties from the 86%, are not associated with foreshock structures, and form mainly downstream of the ULF foreshock boundary. Instead, they display some features of quasi-perpendicular magnetosheath plasma, such as high temperature anisotropy and enhanced magnetic field and velocity in the direction transverse to the shock front. They differ from jets observed by spacecraft in the quasi-perpendicular magnetosheath, however, in having enhanced density. These properties indicate that they might form behind a part of the bow shock that locally and temporarily changes from quasi-parallel to quasi-perpendicular. While jets that propagate flankward are not expected to have direct effects on the magnetosphere by impacting the magnetopause, these results advance our understanding of the effects that bow shock reformation can have in the magnetosheath.

Code and data availability. Vlasiator is distributed under the GPL-2 open-source license. Vlasiator uses a data structure developed in-house. The Analysator software (Battarbee et al., 2021) was used to produce the presented figures. The runs described here can be either run with the above-mentioned code using the boundary conditions reported in this paper, or the data sets can be downloaded from the University of Helsinki servers where they are stored (Pfau-Kempf et al., 2021b).

Author contributions. Conceptualisation: JS, MP. Data curation: JS. Formal analysis: JS. Funding acquisition: JS, MP, LT, YP. Investigation: JS, MP, LT, MB. Methodology: JS, MP, LT, MB. Project administration: MP. Resources: MP, YP, UG, MB. Software: MB, LT, YP, UG. Supervision: MP. Validation: JS, LT, MB. Visualisation: JS. Writing – original draft preparation: JS. Writing – review & editing: JS, LT, MB, MP, YP, HG, MD, FT, HZ, VT, GC, KP, EG.

Competing interests. At least one of the (co-)authors is a member of the editorial board of Annales Geophysicae. The peer-review process was guided by an independent editor, and the authors have also no other competing interests to declare.

Acknowledgements. We acknowledge the European Research Council for Starting grant 200141-QuESpace, with which Vlasiator (Pfau-Kempf et al., 2021a) was developed, and Consolidator grant 682068-PRESTISSIMO, awarded to further develop Vlasiator and use it for scientific investigations. We gratefully acknowledge the Academy of Finland grant nos. 312351, 309937, 328893, 322544, and 339756, and the Horizon 2020 FRoST grant no. 704681. The CSC – IT Center for Science in Finland and the PRACE Tier-0 supercomputer infrastructure in HLRS Stuttgart (grant nos. PRACE-2012061111 and PRACE-2014112573) are acknowledged as they made these results possible. The authors also wish to thank the Finnish Computing Competence Infrastructure (FCCI) for supporting this project with computational and data storage resources. LT acknowledges support from the Academy of Finland (grant number 322544) and from the University of Helsinki (three-year research project RESSAC 2020-2022).

References

Amata, E., Savin, S. P., Ambrosino, D., Bogdanova, Y. V., Marcucci, M. F., Romanov, S., and Skalsky, A.: High Kinetic Energy Density Jets in the Earth's Magnetosheath: A Case Study, Planetary and Space Science, 59, 482–494, https://doi.org/10.1016/j.pss.2010.07.021, 2011.

Andrés, N., Meziane, K., Mazelle, C., Bertucci, C., and Gómez, D.: The ULF Wave Foreshock Boundary: Cluster Observations, Journal of Geophysical Research: Space Physics, 120, 4181–4193, https://doi.org/10.1002/2014JA020783, 2015.

Archer, M., Horbury, T. S., Lucek, E. A., Mazelle, C., Balogh, A., and Dandouras, I.: Size and Shape of ULF Waves in the Terrestrial Foreshock, Journal of Geophysical Research: Space Physics, 110, https://doi.org/10.1029/2004JA010791, 2005.

Archer, M. O. and Horbury, T. S.: Magnetosheath Dynamic Pressure Enhancements: Occurrence and Typical Properties, Annales Geophysicae, 31, 319–331, https://doi.org/10.5194/angeo-31-319-2013, 2013.

Archer, M. O., Horbury, T. S., and Eastwood, J. P.: Magnetosheath Pressure Pulses: Generation Downstream of the Bow Shock from Solar Wind Discontinuities, Journal of Geophysical Research: Space Physics, 117, https://doi.org/10.1029/2011JA017468, 2012.

Archer, M. O., Horbury, T. S., Eastwood, J. P., Weygand, J. M., and Yeoman, T. K.: Magnetospheric Response to Magnetosheath Pressure Pulses: A Low-pass Filter Effect, Journal of Geophysical Research: Space Physics, 118, 5454–5466, https://doi.org/10.1002/jgra.50519, 2013.

Battarbee, M., Ganse, U., Pfau-Kempf, Y., Turc, L., Brito, T., Grandin, M., Koskela, T., and Palmroth, M.: Non-Locality of Earth's Quasi-Parallel Bow Shock: Injection of Thermal Protons in a Hybrid-Vlasov Simulation, Annales Geophysicae, 38, 625–643, https://doi.org/10.5194/angeo-38-625-2020, 2020.

Battarbee, M., Hannuksela, O. A., Pfau-Kempf, Y., Alfthan, S. V., Ganse, U., Jarvinen, R., Leo, Suni, J., Alho, M., Lturc, Ilja, Tvbrito, and Grandin, M.: Fmihpc/Analysator: V0.9, Zenodo, https://doi.org/10.5281/ZENODO.4462515, 2021.

Baumjohann, W. and Treumann, R. A.: Basic Space Plasma Physics, London: Imperial College Press, |c1996, https://doi.org/10.1142/p015, 1996.

Blanco-Cano, X., Omidi, N., and Russell, C. T.: Global Hybrid Simulations: Foreshock Waves and Cavitons under Radial Interplanetary Magnetic Field Geometry: FORESHOCK WAVES AND CAVITONS, Journal of Geophysical Research: Space Physics, 114, n/a–n/a, https://doi.org/10.1029/2008JA013406, 2009.

Dimmock, A. P., Nykyri, K., and Pulkkinen, T. I.: A Statistical Study of Magnetic Field Fluctuations in the Dayside Magnetosheath and Their Dependence on Upstream Solar Wind Conditions, Journal of Geophysical Research: Space Physics, 119, 6231–6248, https://doi.org/10.1002/2014JA020009, 2014.

Dmitriev, A. and Suvorova, A.: Traveling Magnetopause Distortion Related to a Large-scale Magnetosheath Plasma Jet: THEMIS and Ground-based Observations, Journal of Geophysical Research, 117, https://doi.org/10.1029/2011ja016861, 2012.

Dmitriev, A. V. and Suvorova, A. V.: Large-Scale Jets in the Magnetosheath and Plasma Penetration across the Magnetopause: THEMIS Observations, Journal of Geophysical Research: Space Physics, 120, 4423–4437, https://doi.org/10.1002/2014JA020953, 2015.

Eastwood, J. P., Balogh, A., Lucek, E. A., Mazelle, C., and Dandouras, I.: Quasi-Monochromatic ULF Foreshock Waves as Observed by the Four-Spacecraft Cluster Mission: 1. Statistical Properties, Journal of Geophysical Research: Space Physics, 110, https://doi.org/10.1029/2004JA010617, 2005a.

Eastwood, J. P., Lucek, E. A., Mazelle, C., Meziane, K., Narita, Y., Pickett, J., and Treumann, R. A.: The Foreshock, Space Science Reviews, 118, 41–94, https://doi.org/10.1007/s11214-005-3824-3, 2005b.

Gary, S.: Electromagnetic Ion/Ion Instabilities and Their Consequences in Space Plasmas: A Review, Space Science Reviews, 56, https://doi.org/10.1007/BF00196632, 1991.

Gingell, I., Schwartz, S. J., Burgess, D., Johlander, A., Russell, C. T., Burch, J. L., Ergun, R. E., Fuselier, S., Gershman, D. J., Giles, B. L., Goodrich, K. A., Khotyaintsev, Y. V., Lavraud, B., Lindqvist, P.-A., Strangeway, R. J., Trattner, K., Torbert, R. B., Wei, H., and Wilder, F.: MMS Observations and Hybrid Simulations of Surface Ripples at a Marginally Quasi-Parallel Shock, Journal of Geophysical Research: Space Physics, 122, https://doi.org/10.1002/2017JA024538, 2017.

Goncharov, O., Gunell, H., Hamrin, M., and Chong, S.: Evolution of High-Speed Jets and Plasmoids Downstream of the Quasi-Perpendicular Bow Shock, Journal of Geophysical Research: Space Physics, 125, e2019JA027 667, https://doi.org/10.1029/2019JA027667, 2020.

Gunell, H., Stenberg Wieser, G., Mella, M., Maggiolo, R., Nilsson, H., Darrouzet, F., Hamrin, M., Karlsson, T., Brenning, N., De Keyser, J., André, M., and Dandouras, I.: Waves in High-Speed Plasmoids in the Magnetosheath and at the Magnetopause, Annales Geophysicae, 32, 991–1009, https://doi.org/10.5194/angeo-32-991-2014, 2014.

Gutynska, O., Sibeck, D. G., and Omidi, N.: Magnetosheath Plasma Structures and Their Relation to Foreshock Processes, Journal of Geophysical Research: Space Physics, 120, 7687–7697, https://doi.org/10.1002/2014JA020880, 2015.

Hao, Y., Lembege, B., Lu, Q., and Guo, F.: Formation of Downstream High-Speed Jets by a Rippled Nonstationary Quasi-Parallel Shock: 2-D Hybrid Simulations, Journal of Geophysical Research: Space Physics, 121, 2080–2094, https://doi.org/10.1002/2015JA021419, 2016.

Hietala, H. and Plaschke, F.: On the Generation of Magnetosheath High-speed Jets by Bow Shock Ripples, Journal of Geophysical Research, 118, 7237–7245, https://doi.org/10.1002/2013ja019172, 2013.

Hietala, H., Laitinen, T. V., Andréeová, K., Vainio, R., Vaivads, A., Palmroth, M., Pulkkinen, T. I., Koskinen, H. E. J., Lucek, E. A., and Rème, H.: Supermagnetosonic Jets behind a Collisionless Quasiparallel Shock, Physical Review Letters, 103, 245 001, https://doi.org/10.1103/PhysRevLett.103.245001, 2009.

Hietala, H., Partamies, N., Laitinen, T. V., Clausen, L. B. N., Facskó, G., Vaivads, A., Koskinen, H. E. J., Dandouras, I., Rème, H., and Lucek, E. A.: Supermagnetosonic Subsolar Magnetosheath Jets and Their Effects: From the Solar Wind to the Ionospheric Convection, Annales Geophysicae, 30, 33–48, https://doi.org/10.5194/angeo-30-33-2012, 2012.

Hietala, H., Phan, T. D., Angelopoulos, V., Oieroset, M., Archer, M. O., Karlsson, T., and Plaschke, F.: In Situ Observations of a Magnetosheath High-Speed Jet Triggering Magnetopause Reconnection, Geophysical Research Letters, 45, 1732–1740, https://doi.org/10.1002/2017GL076525, 2018.

Johlander, A., Battarbee, M., Turc, L., Ganse, U., Pfau-Kempf, Y., Grandin, M., Suni, J., Tarvus, V., Bussov, M., Zhou, H., Alho, M., Dubart, M., George, H., Papadakis, K., and Palmroth, M.: Quasi-parallel Shock Reformation Seen by Magnetospheric Multiscale and Ion-kinetic Simulations, Geophysical Research Letters, https://doi.org/10.1029/2021GL096335, 2022.

Karimabadi, H., Roytershteyn, V., Vu, H. X., Omelchenko, Y. A., Scudder, J., Daughton, W., Dimmock, A., Nykyri, K., Wan, M., Sibeck, D., Tatineni, M., Majumdar, A., Loring, B., and Geveci, B.: The Link between Shocks, Turbulence, and Magnetic Reconnection in Collisionless Plasmas, Physics of Plasmas, 21, 062 308, https://doi.org/10.1063/1.4882875, 2014.

Karlsson, T., Brenning, N., Nilsson, H., Trotignon, J.-G., Vallières, X., and Facsko, G.: Localized Density Enhancements in the Magnetosheath: Three-dimensional Morphology and Possible Importance for Impulsive Penetration, Journal of Geophysical Research: Space Physics, 117, https://doi.org/10.1029/2011JA017059, 2012.

Karlsson, T., Kullen, A., Liljeblad, E., Brenning, N., Nilsson, H., Gunell, H., and Hamrin, M.: On the Origin of Magnetosheath Plasmoids and Their Relation to Magnetosheath Jets, Journal of Geophysical Research: Space Physics, 120, 7390–7403, https://doi.org/10.1002/2015JA021487, 2015.

Koller, F., Plaschke, F., Temmer, M., Preisser, L., Roberts, O. W., and Vörös, Z.: Magnetosheath Jet Formation Influenced by Parameters in Solar Wind Structures, Journal of Geophysical Research: Space Physics, p. e2023JA031339, https://doi.org/10.1029/2023JA031339, 2023.

LaMoury, A. T., Hietala, H., Plaschke, F., Vuorinen, L., and Eastwood, J. P.: Solar Wind Control of Magnetosheath Jet Formation and Propagation to the Magnetopause, Journal of Geophysical Research: Space Physics, 126, https://doi.org/10.1029/2021JA029592, 2021.

Liu, T. Z., Hao, Y., Wilson, L. B., Turner, D. L., and Zhang, H.: Magnetospheric Multiscale Observations of Earth's Oblique Bow Shock Reformation by Foreshock Ultralow-Frequency Waves, Geophysical Research Letters, 48, https://doi.org/10.1029/2020GL091184, 2021.

Lucek, E. A., Constantinescu, D., Goldstein, M. L., Pickett, J., Pinçon, J. L., Sahraoui, F., Treumann, R. A., and Walker, S. N.: The Magnetosheath, Space Science Reviews, 118, 95–152, https://doi.org/10.1007/s11214-005-3825-2, 2005.

Ma, X., Nykyri, K., Dimmock, A., and Chu, C.: Statistical Study of Solar Wind, Magnetosheath, and Magnetotail Plasma and Field Properties: 12+ Years of THEMIS Observations and MHD Simulations, Journal of Geophysical Research: Space Physics, 125, e2020JA028 209, https://doi.org/10.1029/2020JA028209, 2020.

Němeček, Z., Šafránková, J., Přech, L., Sibeck, D. G., Kokubun, S., and Mukai, T.: Transient Flux Enhancements in the Magnetosheath, Geophysical Research Letters, 25, 1273–1276, https://doi.org/10.1029/98GL50873, 1998.

Omelchenko, Y. A., Chen, L.-J., and Ng, J.: 3D Space-Time Adaptive Hybrid Simulations of Magnetosheath High-Speed Jets, Journal of Geophysical Research: Space Physics, n/a, e2020JA029 035, https://doi.org/10.1029/2020JA029035, 2021.

Omidi, N., Berchem, J., Sibeck, D., and Zhang, H.: Impacts of Spontaneous Hot Flow Anomalies on the Magnetosheath and Magnetopause, Journal of Geophysical Research: Space Physics, 121, 3155–3169, https://doi.org/10.1002/2015JA022170, 2016.

Palmroth, M., Ganse, U., Pfau-Kempf, Y., Battarbee, M., Turc, L., Brito, T., Grandin, M., Hoilijoki, S., Sandroos, A., and von Alfthan, S.: Vlasov Methods in Space Physics and Astrophysics, Living Reviews in Computational Astrophysics, 4, 1, https://doi.org/10.1007/s41115-018-0003-2, 2018a.

Palmroth, M., Hietala, H., Plaschke, F., Archer, M., Karlsson, T., Blanco-Cano, X., Sibeck, D. G., Kajdic, P., Kajdic, P., Ganse, U., Pfau-Kempf, Y., Battarbee, M., and Turc, L.: Magnetosheath Jet Properties and Evolution as Determined by a Global Hybrid-Vlasov Simulation, Annales Geophysicae, 36, 1171–1182, https://doi.org/10.5194/angeo-36-1171-2018, 2018b.

Palmroth, M., Raptis, S., Suni, J., Karlsson, T., Turc, L., Johlander, A., Ganse, U., Pfau-Kempf, Y., Blanco-Cano, X., Akhavan-Tafti, M., Battarbee, M., Dubart, M., Grandin, M., Tarvus, V., and Osmane, A.: Magnetosheath Jet Evolution as a Function of Lifetime: Global Hybrid-Vlasov Simulations Compared to MMS Observations, Annales Geophysicae, 39, 289–308, https://doi.org/10.5194/angeo-39-289-2021, 2021.

Paschmann, G. and Daly, P. W.: Analysis Methods for Multi-Spacecraft Data. ISSI Scientific Reports Series SR-001, ESA/ISSI, Vol. 1. ISBN 1608-280X, 1998, ISSI Scientific Reports Series, 1, 1998.

Pfau-Kempf, Y., Hietala, H., Milan, S. E., Juusola, L., Hoilijoki, S., Ganse, U., von Alfthan, S., and Palmroth, M.: Evidence for Transient, Local Ion Foreshocks Caused by Dayside Magnetopause Reconnection, Annales Geophysicae, 34, 943–959, https://doi.org/10.5194/angeo-34-943-2016, 2016.

Pfau-Kempf, Y., Von Alfthan, S., Sandroos, A., Ganse, U., Koskela, T., Battarbee, M., Hannuksela, O. A., Ilja, Papadakis, K., Grandin, M., Pokhotelov, D., Zhou, H., Leo, and Alho, M.: Fmihpc/Vlasiator: Vlasiator 5.1, Zenodo, https://doi.org/10.5281/ZENODO.4719554, 2021a.

Pfau-Kempf, Y., Von Alfthan, S., Sandroos, A., Ganse, U., Koskela, T., Battarbee, M., Hannuksela, O. A., Ilja, Papadakis, K., Grandin, M., Pokhotelov, D., Zhou, H., Leo, and Alho, M.: Vlasiator Simulation Data (Runs ABA, ABC, AEA, AEC), http://urn.fi/urn:nbn:fi:att:b508942a-ffc0-4e21-8b8b-b91fcfdbd6ee, 2021b.

Plaschke, F. and Hietala, H.: Plasma Flow Patterns in and around Magnetosheath Jets, Annales Geophysicae, 36, 695–703, https://doi.org/10.5194/angeo-36-695-2018, 2018.

Plaschke, F., Hietala, H., and Angelopoulos, V.: Anti-Sunward High-Speed Jets in the Subsolar Magnetosheath, Annales Geophysicae, 31, 1877–1889, https://doi.org/10.5194/angeo-31-1877-2013, 2013.

Plaschke, F., Hietala, H., Angelopoulos, V., and Nakamura, R.: Geoeffective Jets Impacting the Magnetopause Are Very Common, Journal of Geophysical Research: Space Physics, 121, 3240–3253, https://doi.org/10.1002/2016JA022534, 2016.

Plaschke, F., Karlsson, T., Hietala, H., Archer, M., Vörös, Z., Vörös, Z., Z. Voros, Nakamura, R., Magnes, W., Baumjohann, W., Torbert, R. B., Russell, C. T., and Giles, B. L.: Magnetosheath High-Speed Jets: Internal Structure and Interaction with Ambient Plasma†, Journal of Geophysical Research, 122, 10 157–10 175, https://doi.org/10.1002/2017ja024471, 2017.

Plaschke, F., Hietala, H., Archer, M., Blanco-Cano, X., Kajdic, P., Karlsson, T., Lee, S. H., Omidi, N., Palmroth, M., Roytershteyn, V., Schmid, D., Sergeev, V., and Sibeck, D.: Jets Downstream of Collisionless Shocks, Space Science Reviews, 214, 81, https://doi.org/10.1007/s11214-018-0516-3, 2018.

Plaschke, F., Hietala, H., and Vörös, Z.: Scale Sizes of Magnetosheath Jets, Journal of Geophysical Research: Space Physics, 125, e2020JA027 962, https://doi.org/10.1029/2020JA027962, 2020.

Raptis, S., Karlsson, T., Plaschke, F., Kullen, A., and Lindqvist, P.-A.: Classifying Magnetosheath Jets Using MMS: Statistical Properties, Journal of Geophysical Research-Space Physics, 125, e2019JA027 754, https://doi.org/10.1029/2019JA027754, 2020.

Raptis, S., Karlsson, T., Vaivads, A., Lindberg, M., Johlander, A., and Trollvik, H.: On Magnetosheath Jet Kinetic Structure and Plasma Properties, Geophysical Research Letters, 49, e2022GL100 678, https://doi.org/10.1029/2022GL100678, 2022a.

Raptis, S., Karlsson, T., Vaivads, A., Pollock, C., Plaschke, F., Johlander, A., Trollvik, H., and Lindqvist, P.-A.: Downstream High-Speed Plasma Jet Generation as a Direct Consequence of Shock Reformation, Nature Communications, 13, 598, https://doi.org/10.1038/s41467-022-28110-4, 2022b.

Savin, S., Amata, E., Zelenyi, L., Budaev, V., Consolini, G., Treumann, R., Lucek, E., Safrankova, J., Nemecek, Z., Khotyaintsev, Y., Andre, M., Buechner, J., Alleyne, H., Song, P., Blecki, J., Rauch, J. L., Romanov, S., Klimov, S., and Skalsky, A.: High Energy Jets in the Earth's Magnetosheath: Implications for Plasma Dynamics and Anomalous Transport, JETP Letters, 87, 593–599, https://doi.org/10.1134/S0021364008110015, 2008.

Savin, S., Amata, E., Zelenyi, L., Lutsenko, V., Safrankova, J., Nemecek, Z., Borodkova, N., Buechner, J., Daly, P. W., Kronberg, E. A., Blecki, J., Budaev, V., Kozak, L., Skalsky, A., and Lezhen, L.: Super Fast Plasma Streams as Drivers of Transient and Anomalous Magnetospheric Dynamics, Annales Geophysicae, 30, 1–7, https://doi.org/10.5194/angeo-30-1-2012, 2012.

Schwartz, S. J.: Shock and Discontinuity Normals, Mach Numbers, and Related Parameters, ISSI Scientific Reports Series, 1, 249–270, 1998.

Schwartz, S. J. and Burgess, D.: Quasi-Parallel Shocks: A Patchwork of Three-Dimensional Structures, Geophysical Research Letters, 18, 373–376, https://doi.org/10.1029/91GL00138, 1991.

Suni, J., Palmroth, M., Turc, L., Battarbee, M., Johlander, A., Tarvus, V., Alho, M., Bussov, M., Dubart, M., Ganse, U., Grandin, M., Horaites, K., Manglayev, T., Papadakis, K., Pfau-Kempf, Y., and Zhou, H.: Connection Between Foreshock Structures and the Generation of Magnetosheath Jets: Vlasiator Results, Geophysical Research Letters, 48, https://doi.org/10.1029/2021GL095655, 2021.

https://doi.org/10.5194/angeo-2023-14
Preprint. Discussion started: 11 May 2023

Turc, L., Ganse, U., Pfau-Kempf, Y., Hoilijoki, S., Battarbee, M., Juusola, L., Jarvinen, R., Brito, T., Grandin, M., and Palmroth, M.: Foreshock Properties at Typical and Enhanced Interplanetary Magnetic Field Strengths: Results From Hybrid-Vlasov Simulations, Journal of Geophysical Research: Space Physics, 123, 5476–5493, https://doi.org/10.1029/2018JA025466, 2018.

Turc, L., Roberts, O. W., Verscharen, D., Dimmock, A. P., Kajdič, P., Palmroth, M., Pfau-Kempf, Y., Johlander, A., Dubart, M., Kilpua, E. K. J., Soucek, J., Takahashi, K., Takahashi, N., Battarbee, M., and Ganse, U.: Transmission of Foreshock Waves through Earth's Bow Shock, Nature Physics, 19, 78–86, https://doi.org/10.1038/s41567-022-01837-z, 2023.

Vuorinen, L., Hietala, H., and Plaschke, F.: Jets in the Magnetosheath: IMF Control of Where They Occur, Annales Geophysicae, 37, 689–697, https://doi.org/10.5194/angeo-37-689-2019, 2019.

Wang, B., Nishimura, Y., Hietala, H., Lyons, L., Angelopoulos, V., Plaschke, F., Ebihara, Y., and Weatherwax, A.: Impacts of Magnetosheath High-Speed Jets on the Magnetosphere and Ionosphere Measured by Optical Imaging and Satellite Observations, Journal of Geophysical Research: Space Physics, 123, 4879–4894, https://doi.org/10.1029/2017JA024954, 2018.

Wang, B., Nishimura, Y., Hietala, H., and Angelopoulos, V.: Investigating the Role of Magnetosheath High-Speed Jets in Triggering Dayside Ground Magnetic Ultra-Low Frequency Waves, Geophysical Research Letters, 49, https://doi.org/10.1029/2022GL099768, 2022.

Wilson, L. B.: Low Frequency Waves at and Upstream of Collisionless Shocks, in: Geophysical Monograph Series, edited by Keiling, A., Lee, D.-H., and Nakariakov, V., pp. 269–291, John Wiley & Sons, Inc, Hoboken, NJ, https://doi.org/10.1002/9781119055006.ch16, 2016.

Wilson, L. B., Sibeck, D. G., Breneman, A. W., Contel, O. L., Cully, C., Turner, D. L., Angelopoulos, V., and Malaspina, D. M.: Quantified Energy Dissipation Rates in the Terrestrial Bow Shock: 1. Analysis Techniques and Methodology, Journal of Geophysical Research: Space Physics, 119, 6455–6474, https://doi.org/10.1002/2014JA019929, 2014.

Winterhalter, D. and Kivelson, M. G.: Observations of the Earth's Bow Shock under High Mach Number/High Plasma Beta Solar Wind Conditions, Geophysical Research Letters, 15, 1161–1164, https://doi.org/10.1029/GL015i010p01161, 1988.

Zhang, H., Zong, Q., Connor, H., Delamere, P., Facskó, G., Han, D., Hasegawa, H., Kallio, E., Kis, Á., Le, G., Lembège, B., Lin, Y., Liu, T., Oksavik, K., Omidi, N., Otto, A., Ren, J., Shi, Q., Sibeck, D., and Yao, S.: Dayside Transient Phenomena and Their Impact on the Magnetosphere and Ionosphere, Space Science Reviews, 218, 40, https://doi.org/10.1007/s11214-021-00865-0, 2022.